High Versatility and Stability of Mechanochemically Synthesized Halide Perovskite Powders for Optoelectronic Devices

Nico Leupold,[†] Konstantin Schötz,[⊥] Stefania Cacovich,[‡] Irene Bauer,[⊥] Maximilian Schultz,[⊥] Monika Daubinger,[†] Leah Kaiser,[†] Amelle Rebai,[‡] Jean Rousset,[‡,#] Anna Köhler,[⊥,§] Philip Schulz,[‡,◊] Ralf Moos,[†] Fabian Panzer[⊥,]*

[†]Department of Functional Materials, University of Bayreuth, 95440 Bayreuth, Germany

[⊥]Soft Matter Optoelectronics, University of Bayreuth, 95440 Bayreuth, Germany

[§]Bayreuth Institute of Macromolecular Research (BIMF) and Bavarian Polymer Institute (BPI), University of Bayreuth, 95440 Bayreuth, Germany.

[‡]IPVF, Institut Photovoltaïque d'Ile de France (IPVF), 30 route départementale 128, 91120, Palaiseau, France

[#]EDF R&D, 30 route départementale 128, 91120, Palaiseau, France

[◊] CNRS, Institut Photovoltaïque d'Ile de France (IPVF), UMR 9006, 30 route départementale 128, 91120, Palaiseau, France

Keywords: ball milling, MAPbI, passivation, solar cell, strain, hybrid perovskite

Abstract

We show that mechanochemically synthesized halide perovskite powders from a ball milling approach can be employed to fabricate a variety of lead halide perovskites with exceptional intrinsic stability. Our $MAPbI_3$ powder exhibits higher thermal stability than conventionally processed thin-films, without degradation after more than two and a half years of storage and only negligible degradation after heat treatment at 220°C for 14 hours. We further show facile recovery strategies of non-phase-pure powders by simple re-milling or mild heat treatment. Moreover, we demonstrate the mechanochemical synthesis of phase-pure mixed perovskite powders such as $(Cs_{0.05}FA_{0.95}PbI_3)_{0.85}(MAPbBr_3)_{0.15}$ from either the individual metal and organic halides, or from readily prepared ternary perovskites, regardless of the precursor phase purity. Adding KI to the milling process successfully passivated the powders. We also succeeded in preparing a precursor solution on the basis of the powders and obtained uniform thin films from spin-coating this solution. This knowledge was used for efficient solar cells. We find the KI passivation remains in the devices, leading to improved performance and significantly reduced hysteresis. Our work thus demonstrates the potential of mechanochemically synthesized halide perovskite powders for long-time storage and upscaling, further paving the way towards commercialization of perovskite based optoelectronic devices.

1. Introduction

Optoelectronic devices based on (hybrid organic/inorganic) halide perovskites as active semiconductor material have undergone a remarkable development within the past few years. The efficiencies of the current flagship application - perovskite-based solar cells (PSCs) - are now at 24.2 % and thus on a par with those of classic silicon-based solar cells.[1] This development is accompanied by continuous improvements in device stability, which seem to bring the commercialization of PSCs within reach.[2–4] While much of the current enthusiasm for halide perovskites is also due to their ability for versatile processing, e.g., from solution or by evaporation, these processing routes are considerably more complex compared to the corresponding processing approaches of, for example, organic semiconductors. This is because the actual crystallization of the target material, namely the perovskite and its film formation, are inevitably coupled to each other. That is, they always take place simultaneously and thus need to be considered and optimized in parallel. This can be seen as one of the reasons for the typically low reproducibility of the film formation and large arbitrary scattering of device performance even for the same lab,[5] which is a major obstacle to an industrial uptake.

Both, solution processing and co-evaporation typically suffer from a rather limited control of the precursor stoichiometry and, especially on a large scale, from relatively high variations of the surface roughness and the height profile across the module. Furthermore, in the case of co-evaporation, microstructure control is often limited, while for solution-based processing, most of the suitable solvents are considerably toxic, representing a significant safety concern for commercialization.[6]

An alternative synthesis route that is decoupled from the layer formation is the mechanochemical synthesis of halide perovskite powders by simply grinding the reactants into powder form. This can be done, e.g., by using, a high-energy ball mill,[7,8] and this procedure was successfully

demonstrated for various lead containing[9–12] and lead free[13,14] halide perovskite compositions. Beneficial aspects of using perovskite powders were shown, including a superior storage stability of powders compared to their stock solution counterparts.[15] Furthermore, dry synthesis approaches for perovskite powders allow for an extended range of possible reactants that can be used, as no solubility issues do exist.[16] The high level of control of the precursor stoichiometry translates to a high level of control in the overall synthesis, which is also beneficial for improved device properties, when dissolving the thus-prepared perovskite powders for solution-based thin film processing.[8,10,11,17] Also efficient X-ray detectors were demonstrated by directly processing solution based perovskite powders to form a thick layer without the use of solvents,[18] further emphasizing the versatile potential of halide perovskite powders.

Concerning the mechanochemical synthesis of perovskite powders, the correlation of the reactant properties and synthesis parameters with the structural and optoelectronic properties of the final perovskite powders has, however, not yet been addressed in detail. In this study, we investigate the intrinsic stability of mechanochemically synthesized powders and their resilience against external stress (e.g. light, oxygen, humidity), which are crucial aspects for commercial deployment.

The paper is structured as follows. In section 2.1 we demonstrate the impact that milling time and the reactant properties have on the perovskite powder. Section 2.2 we investigate the exceptional stability of these powders against decomposition, and section 2.3 shows that phase pure perovskites powders can be obtained by simple re-milling in case of a prior incomplete conversion or in case of inadvertent degradation, section 2.4 demonstrates that the mechanochemical approach offers a high versatility in the synthesis of more complex multinary mixed perovskites as well as for passivation by the addition of potassium iodide (KI). The electrical properties of the powders and of thin-film solar cells made from dissolved powder are explored in section 2.5. A summarizing and evaluating discussion is concluding the paper.

2. Results and Discussion

2.1 Impact of processing parameters on mechanochemically synthesized perovskite powders

Figure 1 shows the basic principle of the ball milling process for producing perovskite powders. The reactants, e.g. methylammonium iodide (MAI) and lead iodide (PbI_2) powders for the synthesis of the model hybrid perovskite methylammonium lead iodide ($MAPbI_3$), are weighed to the desired stoichiometry and transferred to a milling jar. The jar also contains milling balls and a sufficient amount of cyclohexane, serving as a milling agent but not taking part in the chemical reaction (Figure 1a). Afterwards, the jar is tightly closed and mounted into the ball milling machine. In a planetary ball mill as used in this study, the jar performs two movements: a rotation around its own axis and a rotation around the center of the main disk, on which additional jars can be mounted (Figure 1b).

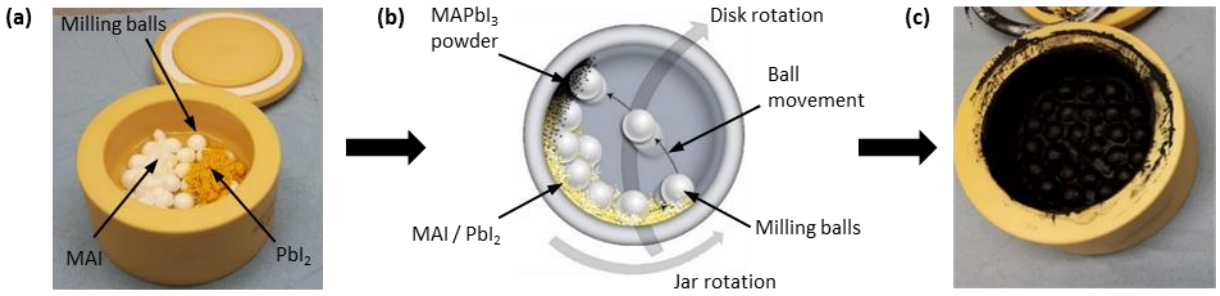

Figure 1. (a) Photograph of a milling jar loaded with milling balls, MAI and PbI_2 precursor powders. (b) Schematic of the ball milling procedure for the mechanochemical synthesis of perovskite powders. (c) Photograph of the milling jar from (a) after the ball milling process and successful mechanochemical synthesis of black $MAPbI_3$ powder.

The combination of these rotational movements leads to a repeated detaching and subsequent tossing of the balls with high energy to the opposing wall. There, they collide with the blended reactant-particles and other balls, providing the energy for the reaction to the desired perovskite. In detail, the mechanochemical synthesis of halide perovskites has been explained by the fact that

during the milling, MAI can be plastically deformed, while PbI_2 is brittle.[19] The distortion of MAI leads to the formation of voids and cracks in the MAI particles,[20] so that PbI_2 particles are pushed into the MAI by the milling balls, being beneficial for the mechanochemical reaction.[19] Additionally, the powders are continuously mixed by the movement of the balls. This ensures a homogenous distribution of all elements in the resulting perovskite. Since cyclohexane has a high vapor pressure, it can be removed within 15 min by evaporation at room temperature. As a last preparation step, the powder is sieved with a 90 µm sieve, where remaining particles are passed through the sieve using a metal spatula, resulting in a fine, free-flowing powder. For the powders that we produce in this study, typical amounts were in the range of 25-30 g per batch.

Figure 2a shows scanning electron microscope (SEM) images of mechanochemically synthesized $MAPbI_3$ powder with a milling time of 60 minutes at different magnifications. The powder in general consists of porous 20-100 µm sized agglomerates of smaller particles. At higher magnification, it becomes clear that the smaller particles are best characterized as compact aggregates in the range of a few µm, which in turn consist of small primary particles in the sub-µm range.[21] To investigate the impact of the milling time on the resulting powder properties, we produced three $MAPbI_3$ powders differing in their milling time (30 min, 60 min and 90 min). From SEM-images (Figure 2b), we can identify a decrease of both, aggregate and primary particle size with milling time, where primary particles are well above 1 µm after 30 min of milling, decreasing to below 1 µm after 60 min, and even reducing to less than 300 nm after 90 minutes of milling.

In the case of $MAPbI_3$, we find the minimum milling time for a complete conversion of $MAPbI_3$ for our synthesis conditions to be 15 minutes, as is confirmed by X-ray diffraction (XRD) measurements (see Figure 2d). However, we could identify a clear impact of the MAI precursor particle size on the minimum milling time needed for a full perovskite conversion. When coarse-grained MAI with particle sizes in the range of a few mm was used, we find reflexes at $2\theta = 12.6°$,

25.2°, 34.2° and 39.5° in the XRD pattern (Figure 2c top panel) after a milling time of 50 minutes, which are associated to residual PbI_2, proofing an incomplete perovskite synthesis.

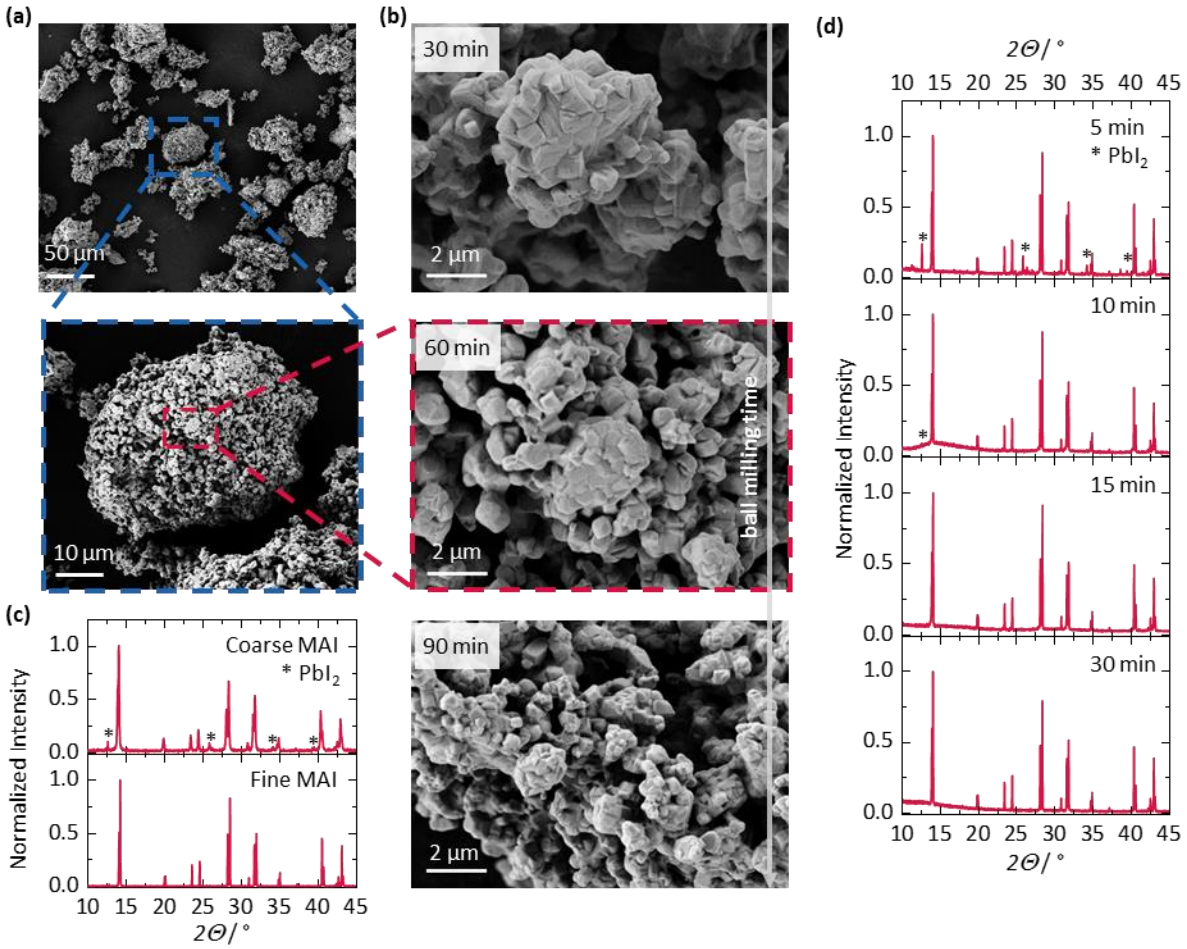

Figure 2. (a) SEM images of mechanochemically synthesized $MAPbI_3$ powder at different magnifications, as indicated. (b) SEM-images of $MAPbI_3$ powders after 30 min (left), 60 min (center), and 90 min (right) of milling. (c) XRD patterns of $MAPbI_3$ powders after 50 min milling time using coarse MAI and after 30 min using fine MAI as shown by photographs. (d) XRD patterns after different milling times of $MAPbI_3$ powders. Signals from crystalline PbI_2 are indicated with stars.

In contrast, the XRD pattern of the powder on the basis of fine MAI with particle sizes around 50 µm (Figure 2c bottom) shows only the desired peaks associated with $MAPbI_3$ already after 30 minutes of milling. We associate this behavior to the increase of reactive surface for the fine MAI

and leading to a decreased amount of energy that is needed for initial comminution of coarse-grained MAI.

2.2. Thermal and temporal stability of perovskite powders

A critical aspect for the development of perovskite applications is the long-term stability of the perovskite powders. In general, the aggregates and primary particles made by the ball-milling process appear compact, which is known to be beneficial in terms of stability.[22–25] To further explore this aspect, we stored mechanochemically synthesized $MAPbI_3$ powder for more than two and a half years in a glovebox with dry (dew point < -50 °C) and inert atmosphere and measured XRD patterns at the beginning and at the end of the storage time (Figure 3 top panel). Even though all main processing steps were carried out in air, we find absolutely no sign of any degradation products such as crystalline PbI_2, demonstrating the intrinsic long-term stability of $MAPbI_3$ in powder form at room temperature. This is consistent with a recent work that indicates a higher stability of halide perovskites in powder form compared to corresponding precursor solution.[15] Besides, we also observed an improved temporal stability of mechanochemically synthesized formamidinium lead iodide ($FAPbI_3$) powders, with a clear deceleration of the typical transformation from its perovskite α- phase towards its non-perovskite hexagonal δ-phase at ambient conditions (for a detailed discussion see SI, Figure S1).

To also test their thermal stability, we stored phase pure $MAPbI_3$ powders (50 minutes milling time) at 160°C and 220°C for 10 and 14 hours, respectively. The treatments were conducted in air with a relative humidity of at least 20 % at room temperature, corresponding to 0.12 % at 160°C and 0.03 % at 220°C. Figure 3 bottom panel shows corresponding XRD-patterns, where we find no Bragg peaks corresponding to PbI_2 for the heat treatment at 160°C and a nearly negligible intensity of the <001> PbI_2 Bragg peak after the temperature treatment at 220°C for 14 hours (see Figure S2 for details). This behavior proves the exceptional thermal stability of $MAPbI_3$ in powder

form, especially when considering that typically a temperature of even less than 160°C is well sufficient to thermally decompose $MAPbI_3$ thin films within minutes.[26]

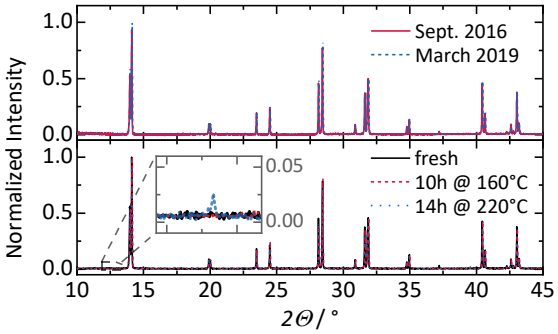

Figure 3. XRD-pattern of $MAPbI_3$ powders before and after more than two and a half years of storage in a dry atmosphere (top panel), and before and after a heat treatment for 10 and 14 hours at 160°C and 220°C in air (bottom panel), with a zoomed region, where the <001> peak of PbI_2 is expected.

Analysis of the XRD-patterns of the $MAPbI_3$ powders with different milling times using the Williamson-Hall method (Figure S3) reveal that the micro strain in the powders is nearly negligible (< 0.01 %). In literature, macro strain levels in perovskite thin films were reported to be in the range from 0.2 to 0.6 % [27] and micro strains to be in the range of 0.1 to 0.2 % [28]. These recent studies also suggest that strain in perovskite thin films is mainly responsible for defect assisted non-radiative recombination and an accelerated degradation of the thin films.[27,28] We thus conclude that the nearly negligible strain we find in the perovskite powders ensures their relatively high stability.

2.3. Regeneration of non-phase-pure powders

A further important aspect for technological purposes is the issue whether non-phase-pure powders can be purified easily. After the heat treatment of $MAPbI_3$ powder at 220°C, we observed

a small degree of thermal degradation, evident from a visible <001> PbI_2 Bragg peak at $2\theta = 12.6°$. However, simply adding a 20 mol % of MAI precursor powder to the degraded $MAPbI_3$ and re-milling this mixture for 50 minutes lead to the full recovery of the $MAPbI_3$ powder, as indicated by the disappearance of the PbI_2 signatures in the corresponding XRD pattern (Figure 4a). We further exploited this possibility of reprocessing perovskite powders to improve their properties. To this end, we re-milled the not yet fully converted $MAPbI_3$ powder where coarse MAI was used (*vide supra*) for additional 30 minutes, which lead to the disappearance of any PbI_2 signal in the XRD pattern (Figure 4b). The same applies to the mechanochemical synthesis of methylammonium lead bromide ($MAPbBr_3$) powder (Figure 4c), where after a first milling step of 50 minutes, we find reflexes in corresponding XRD patterns that are associated to unreacted lead bromide ($PbBr_2$). When milling this powder for 30 min in a second milling step, all traces of $PbBr_2$ are eliminated, indicating a complete conversion of the perovskite.

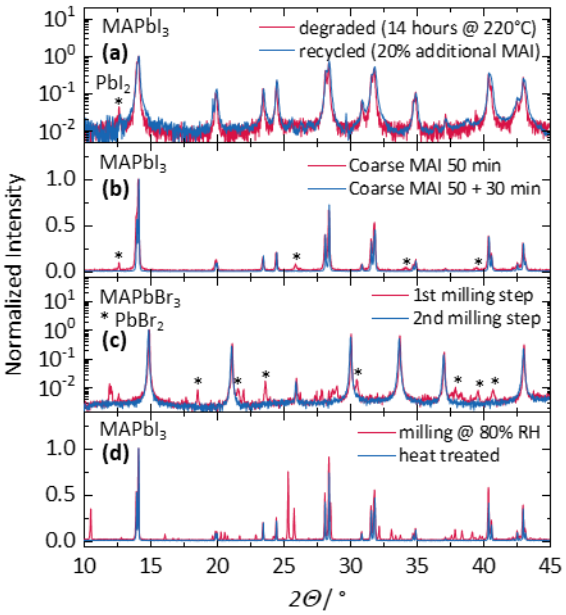

Figure 4. (a) XRD patterns of thermally degraded $MAPbI_3$ powder from Figure 3a (red), and after a milling step, where 20 mol % MAI were added (blue). (b) XRD pattern of $MAPbI_3$ powder using coarse MAI as precursor after 50 minutes of milling (red, from Figure 2c) and after additional 30 minutes of milling (blue). (c) XRD pattern of mechanochemically synthesized $MAPbBr_3$ powder

after a first (50 minutes) and a second re-milling step (30 minutes). Signals from crystalline $PbBr_2$ or PbI_2 are indicated with stars. (d) XRD pattern of $MAPbI_3$ powder synthesized at a high relative humidity of 80 % before and after heat treatment at 120°C for 30 minutes.

If the powders are mechanochemically synthesized at a high relative humidity (rh = 80 %), we could observe several additional reflexes in the corresponding XRD pattern in the case of $MAPbI_3$ (Figure 4d), which are typically associated to the formation of hydrates.[29] By simple mild heating at 120°C for about 30 minutes, it is possible to ensure a complete phase purity of the perovskite, i.e., all additional reflexes have disappeared as evident by XRD.

In overall, our findings demonstrate that ball milling of halide perovskites offers a versatile and easy strategy to recover halide perovskite powders, which also can be beneficial for the development of improved recycling produces of perovskite based optoelectronic devices in the future.

2.4. Versatility in the synthesis of mixed perovskites, including additives

We also addressed the mechanochemical synthesis of state-of-the-art multi-cation mixed halide perovskite,[30,31] to achieve optimized stability and charge transport properties. As a first step, we produced systems whereby only cations ($FA_{0.5}MA_{0.5}PbI_3$) or halides ($MAPbBr_1I_2$) were mixed. The successful synthesis of these different compounds could be confirmed by XRD and their optical properties, demonstrating that the chosen ranges of the milling parameters are also suitable for producing mixed perovskites (see Figure S4 and Table S1 in the SI).

We next explored the possibility to synthesize more complicated material compositions via the ball milling technique. Figure 5a shows the XRD patterns of $(FAPbI_3)_{0.85}(MAPbBr_3)_{0.15}$ and $(Cs_{0.05}FA_{0.95}PbI_3)_{0.85}(MAPbBr_3)_{0.15}$ powders, where no signatures of residuals phases can be observed after 50 minutes of milling. Similar to the case of $MAPbI_3$ powders (Figure 2a), we could

not observe any sign of degradation on the basis of XRD characterizations of the more complex powders after six months of storage under a continuous flow of dry nitrogen inside a desiccator containing a drying agent (Figure S5). For their synthesis, we used the individual precursors, i.e., powders of formamidinium iodide (FAI), PbI_2, methylammonium bromide (MABr), $PbBr_2$ or cesium iodide (CsI) in the appropriate stoichiometric ratios. In the case of $(FAPbI_3)_{0.85}(MAPbBr_3)_{0.15}$, we also explored the possibility to simplify the weighing procedure of the reactants by considering readily prepared mechanochemically synthesized powders of ternary $FAPbI_3$ and $MAPbBr_3$ and use them as starting materials for the mechanochemical synthesis of the mixed perovskite. By doing so, we achieve fully synthesized $(FAPbI_3)_{0.85}(MAPbBr_3)_{0.15}$ already after a milling time of 30 minutes, even independent on whether the $FAPbI_3$ used was in its perovskite α-phase or in its degraded, non-perovskite δ-phase, which nicely emphasizes the versatility of the ball milling approach (Figure 5a).

The elimination of non-radiative recombination pathways by passivation of traps is a known aspect in inorganic semiconductors,[32,33] and is currently becoming an promising research focus also in the field of halide perovskites.[34–36] Recently, it was demonstrated that $(Cs_{0.05}FA_{0.95}PbI_3)_{0.15}(MAPbBr_3)_{0.85}$ can be passivated by adding potassium iodide (KI) to the precursor solution, improving the optoelectronic properties of the perovskite layer and thus device efficiency.[37] To explore this possibility in the context of ball milling and perovskite powders, we used $(FAPbI_3)_{0.85}(MAPbBr_3)_{0.15}$ and $(Cs_{0.05}FA_{0.95}PbI_3)_{0.85}(MAPbBr_3)_{0.15}$, added 5 or 10 mol % solid KI respectively and re-milled these powders for 50 minutes.

Figure 5b shows reflectance and photoluminescence (PL) spectra before and after the passivation of the powders. The passivated powders show an increased PL intensity compared to the non-passivated ones. This behavior was reported as an unambiguous signature of a successful passivation, where non-radiative recombination is reduced, resulting in an increased

photoluminescence quantum efficiency.[32,33,38–40] Complementary, the reflectance measurements show that the band-gap of the passivated powders is slightly shifted to the red with respect to their non-passivated counterparts. This has been reported as a consequence of the passivation of this compound with KI, since the I/Br ratio of the perovskite is slightly increased.[37]

To probe whether the passivation of the perovskite powders occurred homogeneously, energy dispersive X-ray spectroscopy (EDX) was performed. This technique allows to detect the spatial distribution of individual elements such as lead, bromine and potassium. Exemplary spectra are shown in Figure 5c for passivated $(Cs_{0.05}FA_{0.95}PbI_3)_{0.85}(MAPbBr_3)_{0.15}$ powder that was pressed as a pellet (also see Figure S6).

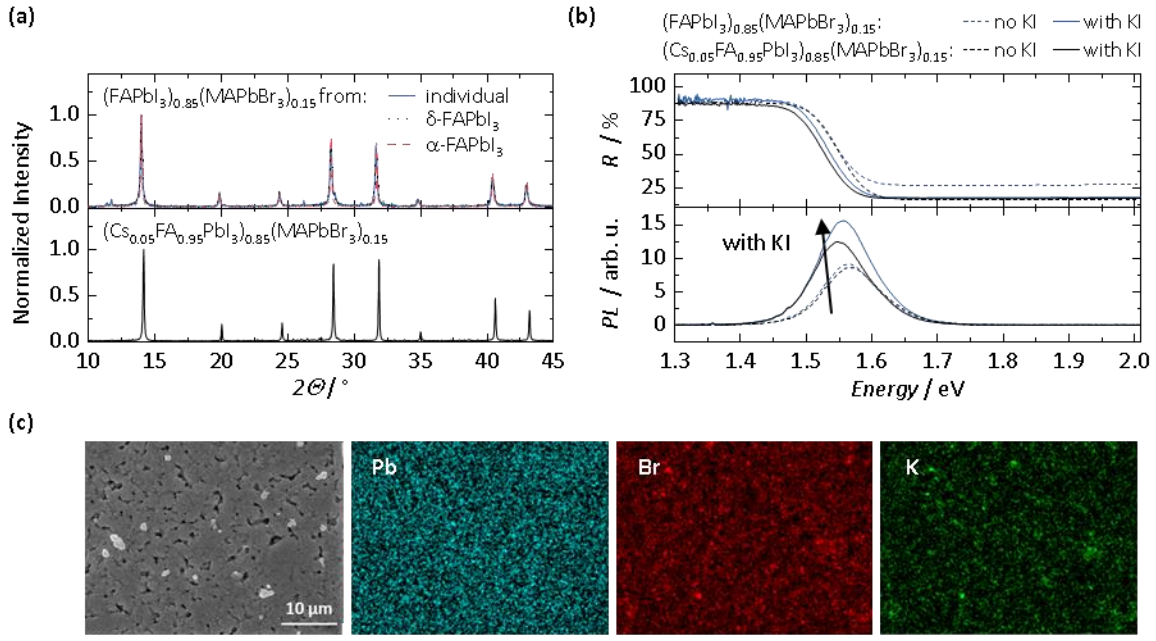

Figure 5. (a) XRD pattern of mechanochemically synthesized $(FAPbI_3)_{0.85}(MAPbBr_3)_{0.15}$ and $(Cs_{0.05}FA_{0.95}PbI_3)_{0.85}(MAPbBr_3)_{0.15}$. (b) Reflectance and photoluminescence spectra of the pure and KI passivated compounds. (c) SEM image and Pb, Br and K mapping obtained via EDX of passivated $(Cs_{0.05}FA_{0.95}PbI_3)_{0.85}(MAPbBr_3)_{0.15}$.

The mapping of the elements shows that potassium is in general evenly distributed over the sample, except for some small areas. There, the EDX signal from potassium and bromine characteristic peaks is more intense, indicating a local enrichment of both elements, which is in accordance with literature.[41] The passivation using KI was suggested to introduce excess iodide into the system, compensating halide vacancies and also attracting and immobilizing additional halides at grain boundaries and surfaces, facilitating the overall electrical properties of the layer.[37]

2.5 Electrical characterization of test devices

An appealing aspect of halide perovskites in powder form is that they allow to separate their synthesis from the actual film formation process. This makes it possible to optimize the synthesis and the film formation independent of each other. For a proof of principle on the electro-optic suitability of these powders, we used various dry powders and pressed them into the shape of cylindrical pellets with 0.5 mm thickness, using a custom-built press setup (see SI for details), and measured their photoresponse. Figure 6 shows the baseline-corrected photoresponse of six perovskite pellets with different stoichiometries, when a bias voltage of 1 V and a low pressure of 2 MPa are applied. A clear photoresponse for all powders can be observed, demonstrating their potential to function as active material in perovskite-based optoelectronic devices that are processed in a solvent-free manner. A detailed discussion about the electrical characterization can be found in the SI (Figure S7).

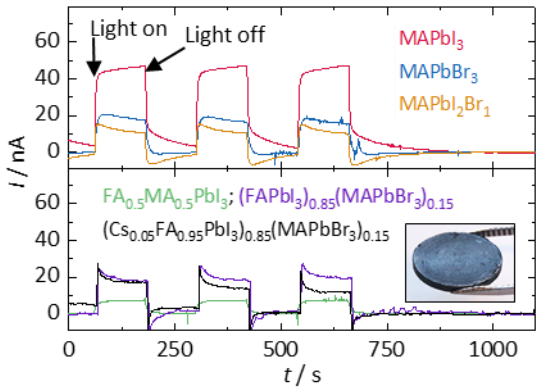

Figure 6. Dark current-corrected temporal photoresponse of different perovskite pellets pressed from their powders upon laser excitation with 405 nm. The top panel shows $MAPbI_3$, $MaPbBr_3$ and $MaPbI_2Br_1$, the bottom panel shows multivalent mixed lead halide perovskites. The inset shows a pellet of $MAPbBr_3$ after the measurement.

However, when it comes to the fabrication of full optoelectronic devices based on perovskite powders, their facile employment in precursors for solution-based thin-film processing of the active layer represents the state of the art.[8,15] We probe the particular use of such a powder-based precursor for the most ubiquitous device architecture of a halide perovskite solar cell. To pursue this goal, we produced perovskite thin-films on top of a SnO_2:F/compact TiO_2/mesoporous TiO_2 (FTO/c-TiO_2/mp-TiO_2) substrates from a 1 M solution of the $(Cs_{0.05}FA_{0.95}PbI_3)_{0.85}(MAPbBr_3)_{0.15}$ powder in dimethyl sulfoxide/dimethylformamide (DMSO:DMF, 4:1 ratio). The thin films were deposited by spin-coating, following an established protocol as described in our previous work.[42] Therein, the thin c-TiO_2 layer acts as a hole blocking layer and the mp-TiO_2 layer as an electron transport layer and scaffold for the perovskite film formation. Our perovskite thin-films derived in this way from the powder precursor solution showed good uniformity and homogeneity as evidenced by XRD and SEM (Figure S8a,b). The optical properties (PL and UV-Vis absorption) are comparable to the plain powder (Figure S8c,d).

We then deposited a hole transport layer comprised of doped 2,2',7,7'-tetrakis [N,N-di(4-methoxyphenyl)amino]-9,9'-spirobifluorene (spiro-OMeTAD) on top of the perovskite film and completed the layer stack by evaporating a gold electrode on top. SEM cross-sectional views of the full photovoltaic device (see Figure 7a) reveal conformal layer growth and a film thickness of about 350 nm, only marginally thinner than our standard device architecture for solar cells comprised of a perovskite layer prepared from a solution of the individual salts (PbI_2, $PbBr_2$, FAI, MAI, and CsI).

In the following, we refer to the device produced from the perovskite powder-based solution as "powder" and the device produced from a solution of the individual salts in our standard process as "reference". We note that the perovskite precursor solution for the reference device had been further optimized by a 10 % excess of PbI_2, which led to higher efficiencies, less hysteresis and longer solar cell lifetimes compared to a corresponding cell from a precursor solution without PbI_2 excess, whereas the powder precursor solution has not been further optimized for this device application.

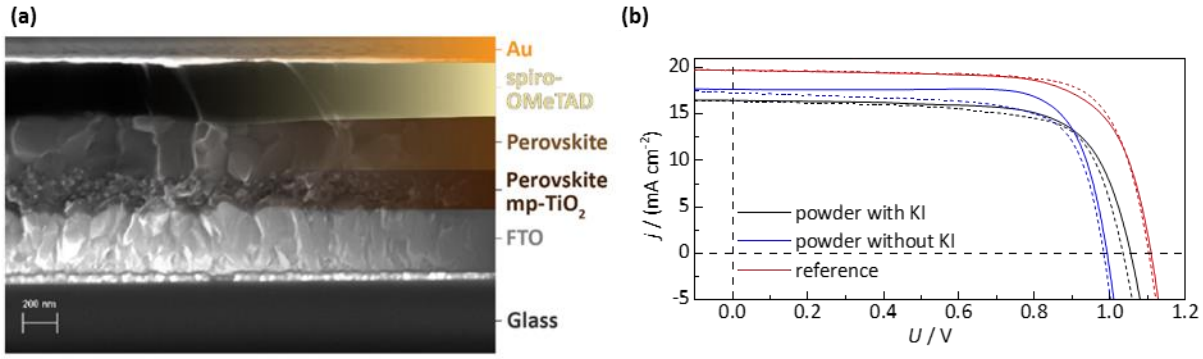

Figure 7. (a) Cross-section SEM image of the completed perovskite powder-based solar cell stack with the perovskite thin film spin-coated of a 1 mol solution of $(Cs_{0.05}FA_{0.95}PbI_3)_{0.85}(MAPbBr_3)_{0.15}$ powder in DMSO:DMF on top of a mp-TiO_2/c-TiO_2/FTO substrate. (b) J-V characteristic of powder-based (with and without KI) and reference perovskite solar cell in forward (full line) and reverse scan direction (dashed line).

The J-V curves of the devices are depicted in Figure 7b and the characteristic solar cell performance parameters sampled over 6 devices for the powder cells and sampled over 3 devices for the reference cells are summarized in Table 1. The powder devices achieved an average power conversion efficiency of 12.4 % (9.4 % in forward scan direction), with a PCE of 13.5 % (12.1 % in forward scan direction) for the champion device (13 % stabilized after 90 s at maximum power point). This value is close to the average PCE of a side-by-side fabricated reference device, which amounts to 14.8 % (15.4 % in forward scan direction) on average and 16.2 % for the champion device, respectively.

Notably, the higher PCE of the reference device can be reasoned by the prior optimization of the precursor formulation by excess PbI_2, also leading to a minimal hysteresis effect. While we succeeded in producing stabilized devices from the perovskite powder solution, these powder devices tend to exhibit a slightly larger hysteresis compared to the reference devices. This manifests in a reduction of the fill factor (FF) in forward scan direction. This effect, together with a lower open circuit voltage (V_{OC}), in the powder devices points to non-ideal interfaces between the perovskite absorber layer and the charge transport layers that leads to increased interface recombination.[43,44] The perovskite film morphology as characterized by SEM looks comparable between films derived from the perovskite powder precursor and the reference perovskite films (Figure S8b). XRD measurements reveal a higher concentration of PbI_2 in the reference films compared to the powder films (Figure S8a). We note that unreacted PbI_2 likely plays a critical role for the higher PCE of the reference devices compared to the powder devices, as PbI_2 has been reported to provide a passivation layer at the device interfaces.[44–46] In addition, we verified that the onset of optical absorption is similar for the reference films and the powder films with and without KI (Figure S8c), while the PL of the thin-films matches to the PL of the powders (Figure S8d).

Table 1. Average PSC device characteristics for $(Cs_{0.05}FA_{0.95}PbI_3)_{0.85}(MAPbBr_3)_{0.15}$ derived from J-V curves (Figure 7b) with values for the champion device in brackets. Detailed statistical data is included in the supplementary information (Figure S9 and Figure S10).

Sample (Champion Device)	J_{sc} **mA/cm²**	V_{OC} **V**	**FF** **%**	**PCE** **%**
Powder without KI / reverse	16.8 (17.62)	1.000 (0.994)	74 (77)	12.4 (13.5)
Powder without KI / forward	16.7 (17.30)	0.970 (0.985)	57 (71)	9.4 (12.1)
Powder with KI / reverse	16.5 (16.45)	1.038 (1.056)	70 (71)	12.1 (12.3)
Powder with KI / forward	16.7 (16.35)	1.050 (1.036)	67 (71)	11.9 (12.0)
Reference / reverse	19.5 (19.70)	1.095 (1.110)	70 (71)	14.8 (15.2)
Reference / forward	19.4 (19.70)	1.090 (1.104)	73 (75)	15.4 (16.2)

Furthermore, the lower short circuit current (J_{SC}) in the powder device compared to the reference device stems from a non-ideal thickness of the absorber layer, which amounts to 350 nm for the powder device and 400 nm for the reference device (Figure S11). The measured J_{SC} has been compared to the integrated current density in external quantum efficiency measurements (Figure S9). Here, we observe a larger mismatch between the currents for the powder devices than for the reference device, which could again be attributed to the lack of excess PbI_2 in the powder films leading to an increase in ion migration and hence differences in the static and dynamic measurements.

We further investigated whether the passivation of the powder by adding KI to the powder precursors for the mechanochemical synthesis would translate to corresponding devices. We compare devices, produced from the KI containing triple-cation perovskite powder, in Figure 7 and

Table 1, to those from the powder without KI and find a systematic increase in V_{OC} by about 50 mV, indicating a passivation of interface defect states. Most remarkably, we achieve a significant reduction of the hysteresis in the devices with KI compared to devices without KI using absorber films from the powder-based solution, which is particularly reflected in the fill factor and in a reduced sensitivity of the device parameters on the scan rate. Again, this behavior is indicative for an improved interface between perovskite and charge transport layers, leading to less recombination and better charge carrier extraction.[44]

3. Summary and Conclusion

In summary, we investigated the mechanochemical synthesis of halide perovskite powders at ambient conditions, identifying the impact of milling time and the influence of the reactant properties on the perovskite powder. We find the mechanochemically synthesized powders to exhibit exceptional stability without any sign of degradation after more than two and a half years of storage, consistent with their intrinsic stability at room temperature, which we correlate to the absence of strain in the powder grains. Their exceptional thermal stability manifests in a nearly negligible amount of PbI_2 formed after heat treatment of $MAPbI_3$ powder at 220°C for 14 hours. In future it will be an interesting aspect to expand the investigations on the correlation between the lack of strain and improved stability of perovskite powders also to other synthesis approaches such as ultra-sonic or precipitation methods. We further demonstrated that we can easily regenerate the perovskites powders in case of a prior incomplete conversion or in case of degradation by simple re-milling. Similarly, hydrated powders, which form when the synthesis is performed at high humidity, can be completely turned to phase-pure powder by soft heat treatment at 120°C for 30 minutes. Following the mechanochemical approach, we successfully synthesized phase-pure multinary mixed perovskites including $(FAPbI_3)_{0.85}(MAPbBr_3)_{0.15}$ and

$(Cs_{0.05}FA_{0.95}PbI_3)_{0.85}(MAPbBr_3)_{0.15}$, which represent state-of-the-art compounds used in highly efficient PSCs. For these multinary compounds, we find their successful synthesis to be independent on whether the individual classic precursors (i.e. MABr, FAI, CsI, PbI_2, $PbBr_2$), or readily prepared perovskite powders of $MAPbBr_3$ and $FAPbI_3$ are used as starting materials. In the latter case, we find that even when using $FAPbI_3$ in its degraded non-perovskite δ-phase, a full synthesis of $(FAPbI_3)_{0.85}(MAPbBr_3)_{0.15}$ remains guaranteed, further proofing the high flexibility of the mechanochemical approach. We also find that these perovskite powders can successfully be passivated by the simple addition of KI in the ball milling process. To assess the functionality in optoelectronic applications, we prepared pellets from the dry powders and demonstrate that all powders show a photoresponse, i.e. a measurable photocurrent. Finally, we dissolved perovskite powder and achieved highly uniform thin-film by spin-coating. Thin-films from the triple-cation perovskite powder were employed to make solar cells in the conventional PSC device geometry, obtaining reliable device characteristics and decent efficiencies on the order of 13% power conversion efficiency (PCE). Even without further optimization, powders with KI additive led to improved device performance and significantly reduced hysteresis compared to powder without KI additive and reference devices from our baseline fabrication process.

Overall, our work demonstrates that the mechanochemical synthesis is well suited to produce a wide variety of highly stable lead halide perovskite powders that meet the demands for solar cell applications. Ball milling is well known to be suitable to the fabrication of larger quantities. The fact that this approach allows for a separate optimization of synthesis and film formation together with the high storage stability and the option to regenerate phase purity by simple re-milling, is likely to pave the way for their utilization especially in an industrially relevant context.

Experimental Section

Powder Preparation

For ball milling the reactants (FAI, MAI, PbI_2, $PbBr_2$) were weighed to the desired stoichiometry (see SI for exact amounts) and transferred into a 80 ml ZrO_2 milling jar containing ZrO_2 milling balls with 10 mm diameter (ball to powder ratio 10:1). At last 11 ml cyclohexane is added as a milling agent. The powders were milled in a Fritsch "Pulverisette 5/4" planetary ball mill at 400 rpm for 5 min, then the milling is paused for 20 min to cool the jar down. The procedure is repeated until the desired milling time is reached.

Powder characterization:

XRD: The structural and phase characterization of the perovskite powders was carried out by reflection mode XRD using a Bruker "D8 Discover A25" with $CuK_{\alpha I}$ radiation (λ = 0.15406 nm), whereby the $K_{\alpha II}$-rays are removed by a Ge -$K_{\alpha I}$-monochromator. The device is operated at 40 kV and 40 mA. The diffractograms were recorded in the 2θ range from 10 to 45° with a 2θ step size of 0.016°.

SEM: The powder morphology was characterized by SEM using a Zeiss Leo 1530 instrument with an accelerating voltage of 3.0 kV. SEM micrographs of perovskite thin-films spin-coated from the powder-based solution and the cross-sections of the completed devices were determined on a Zeiss Merlin VP compact microscope using an acceleration voltage of 15 kV.

Optical characterizations: To measure Photoluminescence spectra, we used a home-built setup. The sample was excited using a 337 nm nitrogen laser (LTB MNL 100). The emitted light was focused into a spectrograph (Andor Shamrock 303i) and detected by a charge-coupled device (CCD) camera (Andor iDus DU420a-OE). The recorded data was corrected by the transmission / reflection of optical components and the efficiency of the CCD camera. Reflectance measurements

were carried out in a commercial UV/VIS-spectrometer (Varian Cary 5000) with an attached integrating sphere for reflectance measurements (External DRA 2500).

Device fabrication:

Fluorine-doped tin oxide (FTO) covered glass substrates (Solems) were cleaned by etching with Zn powder and HCl (4M). The substrates were sonicated for one hour in an RBS® detergent solution (2 vol.-%), rinsed with deionized water and ethanol, and then ultrasonicated in ethanol, dried and annealed to 500°C. Subsequently, a TiO_2 hole blocking layer was prepared by spray pyrolysis deposition (SPD) at 450°C from a precursor solution made of 0.6 mL of titanium diisopropoxide bis(acetyl acetonate) (75 % in 2-propanol, Sigma Aldrich), 0.4 mL of acetyl acetone (Sigma Aldrich) in 9 mL of ethanol as solvent and O_2 as carrier gas. The mesoporous TiO_2 (mp-TiO_2) layer was prepared by spin-coating a solution of TiO_2 paste (30NR-D from Dyesol) in ethanol (1:7 weight ratio) at 4000 rpm for 30 s. The films were then sintered in a sequential heating process (5 min at 125°C, 5 min at 325°C, 5 min at 375°C, 15 min at 450°C and 30 min at 500°C). The samples were finally transferred into a nitrogen filled glove box for the perovskite films processing. Either reference and powder precursor solution were spin-coated onto the mesoporous TiO_2 layers and few seconds later, washed by dripping 0.5 mL of anhydrous diethylether to induce the intermediate adduct formation of the films, as reported previously,[47] from Merck was used as a hole transport material. For the subsequent hole transport layer deposition, 110 mg of Spiro-OMeTAD (2,2',7,7'-tetrakis[*N*,*N*-di(4-methoxyphenyl)amino]-9,9'-spirobifluorene) (Spiro-OMeTAD) from Merck were dissolved in 1 mL of chlorobenzene along with tris(2-(1H-pyrazol-1-yl)-4-tert-butylpyrydine) cobalt(III) bis(trifluoromethylsulphonyl)imide (FK209, Dyesol), lithium bis(trifluoromethyl sulphonyl)imide (LiTFSI, Sigma Aldrich) and 4-*tert*-butylpyridine (*t*-BP, Sigma Aldrich 96% of purity) as additives in relative molar concentrations of 5%, 50% and 330% respectively, with respect to Spiro-OMeTAD. Then, 35 µL of this solution were deposited

by spin coating (3000 rpm for 20 s) on top of the perovskite absorber layer. Finally, 100 nm of gold were thermally evaporated under vacuum as the solar cells top contact.

Perovskite Film Preparation:

In case of the reference devices, the perovskite films were prepared from a $(MA_{0.17}FA_{0.83})Pb(Br_{0.17}I_{0.83})_3$ solution made of 1.10 M PbI_2 (TCI Chemicals), 0.20 M $PbBr_2$ (Alfa Aesar), 1.00 M formamidinium iodide (FAI, dyesol) and 0.20 M methyl ammonium bromide (MABr, Dyesol) in a solvent mixture of DMSO:DMF (4:1 in v/v). The stoichiometry of the optimized films was further altered by adding 10 % of PbI_2 and 5 % CsI to the solution. After vigorous stirring, precursor solution was deposited by spin-coating (first at 2000 rpm to deposit the precursor solution in dynamic mode, then at 6000 rpm while 100 µL of chlorobenzene are applied as anti-solvent). Then, the samples were annealed at 100ºC for 30 min. In case of the layer obtained from the powder, a 1 M precursor solution was prepared dissolving the correct amount of perovskite powder in solvent mixture of DMSO:DMF (4:1 in v/v). After stirring, the solution is centrifuged and then filtered to extract particles that can eventually remained do to incomplete dissolution. The deposition process is the same as previously described for the reference cell.

X-ray Diffractometry: The structural properties of thin film absorbers were characterized by x-ray diffraction measurements in the classical Bragg-Brentano θ-2θ configuration (programmable slit to fix the irradiated area, 0.04° soller slits). The Panalytical Empyrean x-ray diffractometer was operated at 40 kV (40 mA), with Cu-K_α (0.15406 nm) radiation, and including a Cu-Ni filter to suppress the K_β line.

J-V Characterization: Photovoltaic properties of the solar cells were measured under a light source with an AM1.5G spectrum and a calibrated intensity of 1 Sun (100 mW cm^{-2}). A Bio-Logic potentiostat is used to record J-V curves applying a precise scan rate. The voltage sweeping rate was fixed to 20 mV s^{-1} in reverse and forward J-V scans directions. For steady-state output

performance, PCE was plotted as function of time at maximum power point voltage (V_{MPP}) conditions under continuous illumination using the same light source employed for J-V measurements. The Perovskite based cells present an active area of 0.16 cm^2, but the illuminated surface is limited to 0.09 cm^2 with black metal laser-cut mask during the performance measurements.

Supporting Information

The Supporting Information is available free of charge on the ACS Publications website

Experimental details, figures of stability, Photoluminescence measurements, additional device data, discussion on photoresponse behavior (PDF)

Corresponding Author

*E-mail: fabian.panzer@uni-bayreuth.de

Notes

The authors declare no competing financial interest.

Acknowledgement

The authors acknowledge financial support by the German National Science Foundation DFG via the GRK 1640 and via MO 1060/32-1 and by the Bavarian State Ministry of Science, Research, and the Arts for the Collaborative Research Network ‘‘Solar Technologies go Hybrid’’. We further thank the Department of Metal and Alloys and Dr. Johannes Thiessen from the Department of Chemical Engineering for XRD measurements, and Angelika Mergner and the Keylab Electron and Optical Microscopy of the Bavarian Polymer Institute (BPI) for SEM images. This project has been supported by the French Government in the frame of the program of investment for the future (Programme d'Investissement d'Avenir - ANR-IEED-002-01).

References

(1) NREL. Research Cell Record Efficiency Chart. https://www.nrel.gov/pv/cell-efficiency.html (accessed June 3, 2019).

(2) Christians, J. A.; Schulz, P.; Tinkham, J. S.; Schloemer, T. H.; Harvey, S. P.; Tremolet de Villers, B. J.; Sellinger, A.; Berry, J. J.; Luther, J. M. Tailored Interfaces of Unencapsulated Perovskite Solar Cells for >1,000 hour Operational Stability. *Nat. Energy* **2018**, *3*, 68–74.

(3) Grancini, G.; Roldán-Carmona, C.; Zimmermann, I.; Mosconi, E.; Lee, X.; Martineau, D.; Narbey, S.; Oswald, F.; Angelis, F. de; Graetzel, M.; Nazeeruddin, M. K. One-Year Stable Perovskite Solar Cells by 2D/3D Interface Engineering. *Nat. Commun.* **2017**, *8*, 15684.

(4) Tsai, H.; Nie, W.; Blancon, J.-C.; Stoumpos, C. C.; Asadpour, R.; Harutyunyan, B.; Neukirch, A. J.; Verduzco, R.; Crochet, J. J.; Tretiak, S.; Pedesseau, L.; Even, J.; Alam, M. A.; Gupta, G.; Lou, J.; Ajayan, P. M.; Bedzyk, M. J.; Kanatzidis, M. G. High-Efficiency Two-Dimensional Ruddlesden-Popper Perovskite Solar Cells. *Nature* **2016**, *536*, 312–316.

(5) Saliba, M.; Correa-Baena, J.-P.; Wolff, C. M.; Stolterfoht, M.; Phung, N.; Albrecht, S.; Neher, D.; Abate, A. How to Make over 20% Efficient Perovskite Solar Cells in Regular (*n*–*i*–*p*) and Inverted (*p*–*i*–*n*) Architectures. *Chem. Mater.* **2018**, *30*, 4193–4201.

(6) Holliman, P. J.; Jones, E. W.; Connell, A.; Ghosh, S.; Furnell, L.; Hobbs, R. J. Solvent Issues During Processing and Device Lifetime for Perovskite Solar Cells. *Mater. Res. Innovations* **2015**, *19*, 508–511.

(7) Jodlowski, A. D.; Yépez, A.; Luque, R.; Camacho, L.; Miguel, G. de. Benign-by-Design Solventless Mechanochemical Synthesis of Three-, Two-, and One-Dimensional Hybrid Perovskites. *Angew. Chem. Int. Ed.* **2016**, *55*, 14972–14977.

(8) Prochowicz, D.; Franckevičius, M.; Cieślak, A. M.; Zakeeruddin, S. M.; Grätzel, M.; Lewiński, J. Mechanosynthesis of the Hybrid Perovskite $CH_3NH_3PbI_3$: Characterization and the Corresponding Solar Cell Efficiency. *J. Mater. Chem. A* **2015**, *3*, 20772–20777.

(9) Elseman, A. M.; Shalan, A. E.; Rashad, M. M.; Hassan, A. M. Experimental and Simulation Study for Impact of Different Halides on the Performance of Planar Perovskite Solar Cells. *Mater. Sci. Semicond. Process.* **2017**, *66*, 176–185.

(10) Karmakar, A.; Askar, A. M.; Bernard, G. M.; Terskikh, V. V.; Ha, M.; Patel, S.; Shankar, K.; Michaelis, V. K. Mechanochemical Synthesis of Methylammonium Lead Mixed–Halide Perovskites: Unraveling the Solid-Solution Behavior Using Solid-State NMR. *Chem. Mater.* **2018**, *30*, 2309–2321.

(11) Prochowicz, D.; Yadav, P.; Saliba, M.; Saski, M.; Zakeeruddin, S. M.; Lewiński, J.; Grätzel, M. Mechanosynthesis of Pure Phase Mixed-Cation $MA_xFA_{1-x}PbI_3$ Hybrid Perovskites: Photovoltaic Performance and Electrochemical Properties. *Sustainable Energy Fuels* **2017**, *1*, 689–693.

(12) Sadhukhan, P.; Kundu, S.; Roy, A.; Ray, A.; Maji, P.; Dutta, H.; Pradhan, S. K.; Das, S. Solvent-Free Solid-State Synthesis of High Yield Mixed Halide Perovskites for Easily Tunable Composition and Band Gap. *Cryst. Growth Des.* **2018**, *18*, 3428–3432.

(13) Hong, Z.; Tan, D.; John, R. A.; Tay, Y. K. E.; Ho, Y. K. T.; Zhao, X.; Sum, T. C.; Mathews, N.; García, F.; Soo, H. S. Completely Solvent-free Protocols to Access Phase-Pure, Metastable Metal Halide Perovskites and Functional Photodetectors from the Precursor Salts. *iScience* **2019**, *16*, 312–325.

(14) Saski, M.; Prochowicz, D.; Marynowski, W.; Lewiński, J. Mechanosynthesis, Optical, and Morphological Properties of MA, FA, Cs-SnX_3 (X = I, Br) and Phase-Pure Mixed-Halide $MASnI_xBr_{3-x}$ Perovskites. *Eur. J. Inorg. Chem.* **2019**, *2019*, 2680–2684.

(15) Dou, B.; Wheeler, L. M.; Christians, J. A.; Moore, D. T.; Harvey, S. P.; Berry, J. J.; Barnes, F. S.; Shaheen, S. E.; van Hest, M. F.A.M. Degradation of Highly Alloyed Metal Halide Perovskite Precursor Inks: Mechanism and Storage Solutions. *ACS Energy Lett.* **2018**, *3*, 979–985.

(16) Prochowicz, D.; Yadav, P.; Saliba, M.; Kubicki, D. J.; Tavakoli, M. M.; Zakeeruddin, S. M.; Lewiński, J.; Emsley, L.; Grätzel, M. One-step Mechanochemical Incorporation of an Insoluble Cesium Additive for High Performance Planar Heterojunction Solar Cells. *Nano Energy* **2018**, *49*, 523–528.

(17) Prochowicz, D.; Yadav, P.; Saliba, M.; Saski, M.; Zakeeruddin, S. M.; Lewiński, J.; Grätzel, M. Reduction in the Interfacial Trap Density of Mechanochemically Synthesized $MAPbI_3$. *ACS Appl. Mater. Interfaces* **2017**, *9*, 28418–28425.

(18) Shrestha, S.; Fischer, R.; Matt, G. J.; Feldner, P.; Michel, T.; Osvet, A.; Levchuk, I.; Merle, B.; Golkar, S.; Chen, H.; Tedde, S. F.; Schmidt, O.; Hock, R.; Rührig, M.; Göken, M.; Heiss, W.; Anton, G.; Brabec, C. J. High-Performance Direct Conversion X-ray Detectors Based on Sintered Hybrid Lead Triiodide Perovskite Wafers. *Nat. Photonics* **2017**, *11*, 436–440.

(19) Manukyan, K. V.; Yeghishyan, A. V.; Moskovskikh, D. O.; Kapaldo, J.; Mintairov, A.; Mukasyan, A. S. Mechanochemical Synthesis of Methylammonium Lead Iodide Perovskite. *J. Mater. Sci.* **2016**, *51*, 9123–9130.

(20) Jana, A.; Mittal, M.; Singla, A.; Sapra, S. Solvent-free, Mechanochemical Syntheses of Bulk Trihalide Perovskites and their Nanoparticles. *Chem. Commun.* **2017**, *53*, 3046–3049.

(21) Dirk Walter. Primary Particles – Agglomerates – Aggregates. In *Nanomaterials*; Commission for the Investigation of Health Hazards of Chemical Compounds in the Work Area, Ed.; Report; Wiley-VCH: Weinheim, Germany, 2013; pp 9–24.

(22) Gujar, T. P.; Thelakkat, M. Highly Reproducible and Efficient Perovskite Solar Cells with Extraordinary Stability from Robust $CH_3NH_3PbI_3$: Towards Large-Area Devices. *Energy Technol.* **2016**, *4*, 449–457.

(23) Yen, H.-J.; Liang, P.-W.; Chueh, C.-C.; Yang, Z.; Jen, A. K.-Y.; Wang, H.-L. Large Grained Perovskite Solar Cells Derived from Single-Crystal Perovskite Powders with Enhanced Ambient Stability. *ACS Appl. Mater. Interfaces* **2016**, *8*, 14513–14520.

(24) Zhang, J.; Zhao, Y.; Yang, D.; Li, C.; Liu, S. Highly Stabilized Perovskite Solar Cell Prepared Using Vacuum Deposition. *RSC Adv.* **2016**, *6*, 93525–93531.

(25) Wang, B.; Chen, T. Exceptionally Stable $CH_3NH_3PbI_3$ Films in Moderate Humid Environmental Condition. *Adv. Sci.* **2016**, *3*, 1500262.

(26) Gujar, T. P.; Unger, T.; Schönleber, A.; Fried, M.; Panzer, F.; van Smaalen, S.; Köhler, A.; Thelakkat, M. The Role of PbI_2 in $CH_3NH_3PbI_3$ Perovskite Stability, Solar Cell Parameters and Device Degradation. *Phys. Chem. Chem. Phys.* **2017**, *20*, 605–614.

(27) Zhao, J.; Deng, Y.; Wei, H.; Zheng, X.; Yu, Z.; Shao, Y.; Shield, J. E.; Huang, J. Strained Hybrid Perovskite Thin Films and their Impact on the Intrinsic Stability of Perovskite Solar Cells. *Sci. Adv.* **2017**, *3*, eaao5616.

(28) Jones, T. W.; Osherov, A.; Alsari, M.; Sponseller, M.; Duck, B. C.; Jung, Y.-K.; Settens, C.; Niroui, F.; Brenes, R.; Stan, C. V.; Li, Y.; Abdi-Jalebi, M.; Tamura, N.; Macdonald, J. E.; Burghammer, M.; Friend, R. H.; Bulović, V.; Walsh, A.; Wilson, G. J.; Lilliu, S.; Stranks, S. D. Lattice Strain Causes Non-radiative Losses in Halide Perovskites. *Energy Environ. Sci.* **2019**, *12*, 596–606.

(29) Guo, X.; McCleese, C.; Lin, W.-C.; Burda, C. Curing of Degraded $MAPbI_3$ Perovskite Films. *RSC Adv.* **2016**, *6*, 60620–60625.

(30) Saliba, M.; Matsui, T.; Seo, J.-Y.; Domanski, K.; Correa-Baena, J.-P.; Nazeeruddin, M. K.; Zakeeruddin, S. M.; Tress, W.; Abate, A.; Hagfeldt, A.; Grätzel, M. Cesium-Containing Triple Cation Perovskite Solar Cells: Improved Stability, Reproducibility and High Efficiency. *Energy Environ. Sci.* **2016**, *9*, 1989–1997.

(31) Ono, L. K.; Juarez-Perez, E. J.; Qi, Y. Progress on Perovskite Materials and Solar Cells with Mixed Cations and Halide Anions. *ACS Appl. Mater. Interfaces* **2017**, *9*, 30197–30246.

(32) Myung, N.; Bae, Y.; Bard, A. J. Enhancement of the Photoluminescence of CdSe Nanocrystals Dispersed in $CHCl_3$ by Oxygen Passivation of Surface States. *Nano Lett.* **2003**, *3*, 747–749.

(33) van Vugt, L. K.; Veen, S. J.; Bakkers, E. P. A. M.; Roest, A. L.; Vanmaekelbergh, D. Increase of the Photoluminescence Intensity of InP Nanowires by Photoassisted Surface Passivation. *J. Am. Chem. Soc.* **2005**, *127*, 12357–12362.

(34) Brenes, R.; Guo, D.; Osherov, A.; Noel, N. K.; Eames, C.; Hutter, E. M.; Pathak, S. K.; Niroui, F.; Friend, R. H.; Islam, M. S.; Snaith, H. J.; Bulović, V.; Savenije, T. J.; Stranks, S. D. Metal Halide Perovskite Polycrystalline Films Exhibiting Properties of Single Crystals. *Joule* **2017**, *1*, 155–167.

(35) Zheng, X.; Chen, B.; Dai, J.; Fang, Y.; Bai, Y.; Lin, Y.; Wei, H.; Zeng, X. C.; Huang, J. Defect Passivation in Hybrid Perovskite Solar Cells Using Quaternary Ammonium Halide Anions and Cations. *Nat. Energy* **2017**, *2*, 17102.

(36) Niu, T.; Lu, J.; Munir, R.; Li, J.; Barrit, D.; Zhang, X.; Hu, H.; Yang, Z.; Amassian, A.; Zhao, K.; Liu, S. F. Stable High-Performance Perovskite Solar Cells via Grain Boundary Passivation. *Adv. Mater.* **2018**, *30*, e1706576.

(37) Abdi-Jalebi, M.; Andaji-Garmaroudi, Z.; Cacovich, S.; Stavrakas, C.; Philippe, B.; Richter, J. M.; Alsari, M.; Booker, E. P.; Hutter, E. M.; Pearson, A. J.; Lilliu, S.; Savenije, T. J.; Rensmo, H.; Divitini, G.; Ducati, C.; Friend, R. H.; Stranks, S. D. Maximizing and Stabilizing Luminescence from Halide Perovskites with Potassium Passivation. *Nature* **2018**, *555*, 497–501.

(38) Dänekamp, B.; Droseros, N.; Palazon, F.; Sessolo, M.; Banerji, N.; Bolink, H. J. Efficient Photo- and Electroluminescence by Trap States Passivation in Vacuum-Deposited Hybrid Perovskite Thin Films. *ACS Appl. Mater. Interfaces* **2018**, *10*, 36187–36193.

(39) Ahmed, G. H.; El-Demellawi, J. K.; Yin, J.; Pan, J.; Velusamy, D. B.; Hedhili, M. N.; Alarousu, E.; Bakr, O. M.; Alshareef, H. N.; Mohammed, O. F. Giant Photoluminescence Enhancement in $CsPbCl_3$ Perovskite Nanocrystals by Simultaneous Dual-Surface Passivation. *ACS Energy Lett.* **2018**, *3*, 2301–2307.

(40) Lee, S.; Park, J. H.; Lee, B. R.; Jung, E. D.; Yu, J. C.; Di Nuzzo, D.; Friend, R. H.; Song, M. H. Amine-Based Passivating Materials for Enhanced Optical Properties and Performance of Organic-Inorganic Perovskites in Light-Emitting Diodes. *J. Phys. Chem. Lett.* **2017**, *8*, 1784–1792.

(41) Kubicki, D. J.; Prochowicz, D.; Hofstetter, A.; Zakeeruddin, S. M.; Grätzel, M.; Emsley, L. Phase Segregation in Potassium-Doped Lead Halide Perovskites from ^{39}K Solid-State NMR at 21.1 T. *J. Am. Chem. Soc.* **2018**, *140*, 7232–7238.

(42) Bercegol, A.; Ramos, F. J.; Rebai, A.; Guillemot, T.; Ory, D.; Rousset, J.; Lombez, L. Slow Diffusion and Long Lifetime in Metal Halide Perovskites for Photovoltaics. *J. Phys. Chem. C* **2018**, *122*, 24570–24577.

(43) Fakharuddin, A.; Schmidt-Mende, L.; Garcia-Belmonte, G.; Jose, R.; Mora-Sero, I. Interfaces in Perovskite Solar Cells. *Adv. Energy Mater.* **2017**, *7*, 1700623.

(44) Schulz, P.; Cahen, D.; Kahn, A. Halide Perovskites: Is It All about the Interfaces? *Chem. Rev.* **2019**, *119*, 3349–3417.

(45) Liu, F.; Dong, Q.; Wong, M. K.; Djurišić, A. B.; Ng, A.; Ren, Z.; Shen, Q.; Surya, C.; Chan, W. K.; Wang, J.; Ng, A. M. C.; Liao, C.; Li, H.; Shih, K.; Wei, C.; Su, H.; Dai, J. Is Excess PbI_2 Beneficial for Perovskite Solar Cell Performance? *Adv. Energy Mater.* **2016**, *6*, 1502206.

(46) Jacobsson, T. J.; Correa-Baena, J.-P.; Halvani Anaraki, E.; Philippe, B.; Stranks, S. D.; Bouduban, M. E. F.; Tress, W.; Schenk, K.; Teuscher, J.; Moser, J.-E.; Rensmo, H.; Hagfeldt, A. Unreacted PbI_2 as a Double-Edged Sword for Enhancing the Performance of Perovskite Solar Cells. *J. Am. Chem. Soc.* **2016**, *138*, 10331–10343.

(47) Ahn, N.; Son, D.-Y.; Jang, I.-H.; Kang, S. M.; Choi, M.; Park, N.-G. Highly Reproducible Perovskite Solar Cells with Average Efficiency of 18.3% and Best Efficiency of 19.7% Fabricated via Lewis Base Adduct of Lead(II) Iodide. *J. Am. Chem. Soc.* **2015**, *137*, 8696–8699.

TOC:

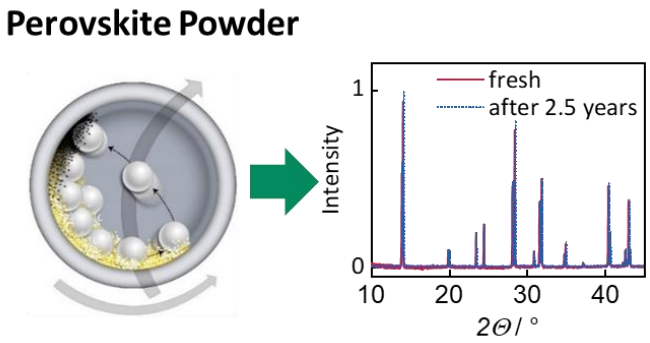
Perovskite Powder
fresh
after 2.5 years
Intensity
1
0
10
20
30
40
2Θ / °